Dynamical separation of spherical bodies in supersonic flow

S. J. LAURENCE[1], N. J. PARZIALE[2], AND R. DEITERDING[3]

[1]Institute of Aerodynamics and Flow Technology, Spacecraft Department, German Aerospace Center, Bunsenstraße 10, 37073 Göttingen, Germany

[2]Graduate Aerospace Laboratories, California Institute of Technology, Pasadena, CA 91125, USA

[3]Oak Ridge National Laboratory, P.O. Box 2008 MS6367, Oak Ridge, TN 37831, USA

(Received ?? and in revised form ??)

An experimental and computational investigation of the unsteady separation behaviour of two spheres in a highly supersonic flow is carried out. The spherical bodies, initially touching, are released with negligible relative velocity, an arrangement representing the idealized binary fragmentation of a meteoritic body in the atmosphere. In experiments performed in a Mach-4 Ludwieg tube, nylon spheres are initially suspended in the test section by weak threads and, following detachment of the threads by the arrival of the flow, fly freely according to the aerodynamic forces experienced. The resulting sphere motions and unsteady flow structures are recorded using high-speed shadowgraphy. The qualitative separation behaviour and the final lateral velocity of the smaller sphere are found to vary strongly with both the radius ratio and the initial alignment angle of the two spheres. More disparate radii and initial configurations in which the smaller sphere centre lies downstream of that of the larger sphere both increase the tendency for the smaller sphere to be entrained within the flow region bounded by the bow-shock of the larger body, rather than expelled from this region. At a critical angle for a given radius ratio (or a critical radius ratio for a given angle), transition from entrainment to expulsion occurs; at this critical value, the final lateral velocity is close to maximum due to the "surfing" effect noted by Laurence & Deiterding (*J. Fluid Mech.*, vol. 676, 2011, pp. 396-431) at hypersonic Mach numbers. A high-precision tracking algorithm is used to provide quantitative comparisons between experiments and high-resolution inviscid numerical simulations, with generally favourable agreement.

Key Words:

---

1. Introduction

The study of aerodynamic interactions between separating bodies in high-speed flow is of interest in such areas as meteoroid fragmentation, the deorbiting of space debris, and launch-vehicle stage separation. With regard to meteoroid fragmentation, the interactions that take place immediately following the atmospheric disruption of a meteoritic body can play a large role in determining, for example, the rate of energy deposition to the atmosphere by an airblast, and thus the damage produced at the terrestrial surface (Hills & Goda 1993), or the fall pattern of fragments that survive the atmospheric

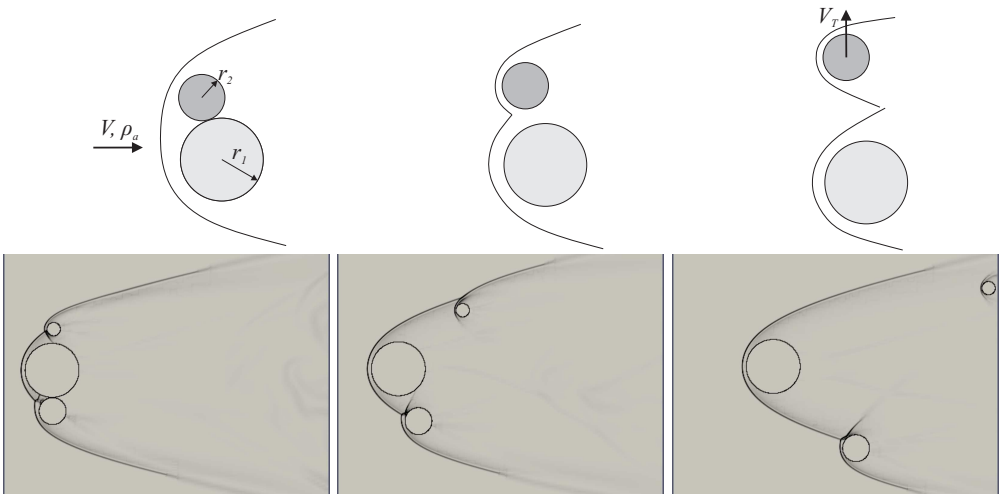

FIGURE 1. (Above) The lateral fragment separation model assumed by Passey & Melosh (1980); (below) the separation behaviour determined by Laurence & Deiterding (2011). In the latter, the larger of the secondary bodies "surfs" downstream on the bow-shock of the main body, whereas the smaller secondary body is quickly entrained within the flow region bounded by the bow-shock.

transit (Passey & Melosh 1980). Models that have been developed to describe the aerodynamics of a fragmenting meteoroid generally fall into one of two categories: hydrodynamic/swarm models, e.g., Chyba *et al.* (1993) and Svetsov *et al.* (1995), appropriate for heavily fragmented bodies; and discrete-fragmentation models to simulate bodies that are disrupted into a limited number of fragments. In the present work we are concerned with the latter type of model.

The first to attempt a systematic analysis of the separation behaviour of discrete fragments were Passey & Melosh (1980), who assumed a purely lateral separation between two fragments of radii $r_1 \geqslant r_2$ (see figure 1). Using simple dimensional arguments, they derived the following scaling law for the final lateral separation velocity, V_T, of the smaller body:

$$V_T = \sqrt{C \frac{r_1}{r_2} \frac{\rho_a}{\rho_m}} V. \tag{1.1}$$

Here V is the velocity of the meteoroid through the atmosphere, ρ_a and ρ_m are the atmospheric and meteoroid densities, respectively, and C is a constant that Passey & Melosh determined through an examination of various terrestrial crater fields to lie between 0.03 and 2.25. Numerical simulations of the symmetrical separation of equally sized bodies were carried out by Artem'eva & Shuvalov (1996) and Artemieva & Shuvalov (2001), yielding values of C in (1.1) of approximately 0.2 and 1 for two and multiple bodies, respectively. These results were incorporated into a model used to simulate specific fragmentation events (Artemieva & Shuvalov 2001; Artemieva & Pierazzo 2009) and to predict, for instance, the rate of arrival of meteoroids at Earth (Bland & Artemieva 2003, 2006).

However, a detailed analysis of a videotaped recording of the Morávka fall (Borovička & Kalenda 2003) revealed serious shortcomings in Artemieva & Shuvalov's model, with measured separation velocities reaching values of up to an order of magnitude larger than those predicted. An explanation for this discrepancy is suggested by the study of Laurence & Deiterding (2011), which demonstrated that findings for equally sized fragments

cannot be accurately extended to the separation behaviour of bodies of different sizes. Laurence & Deiterding also showed that the scaling law of Passey & Melosh, (1.1), does not adequately predict the separation behaviour of unequally sized bodies. This is because, contrary to Passey & Melosh's assumption of a purely lateral separation, the smaller body of the pair (referred to hereinafter as the secondary body) is subject to a higher axial acceleration and thus travels both laterally and downstream relative to the larger (primary) body. This can lead to a phenomenon referred to as "shock-wave surfing", in which the secondary body traces a trajectory so as to follow the bow-shock of the primary body downstream (see figure 1). In doing so, it develops a significantly larger lateral velocity than would otherwise be possible, since, in the surfing configuration, the flow field about the secondary body produces a substantial repulsive lateral force. More specifically, the outer side of the secondary body is exposed to singly shocked flow, whereas the flow on the inner side is processed by the primary bow-shock before passing through the secondary shock, and thus experiences a smaller overall stagnation pressure loss. This leads to higher pressures on the inner-side surface. Bodies smaller than a critical value do not develop a sufficiently high lateral velocity in the initial stages of separation to commence surfing and are quickly entrained within the flow region bounded by the primary bow-shock; in contrast, bodies significantly larger than the critical value are soon expelled from this flow region. Thus, the ratio of body sizes is a crucial parameter in determining the separation behaviour.

The main intent of the present article is to provide an experimental counterpart to the study of Laurence & Deiterding (2011), which was based on numerical simulations and theoretical analysis. The experimental facility employed is the GALCIT Ludwieg tube, capable of producing cold supersonic flows with Mach numbers of up to 4.0. While this is significantly lower than the hypersonic Mach numbers of the earlier study (and which are typical of meteoroid entry), a preliminary numerical investigation indicated that the surfing effect still appears at Mach 4. Thus, an extensive experimental investigation was undertaken to explore the separation characteristics of spherical bodies under such flow conditions. The idealized configuration for the study is that of two initially touching spheres travelling in supersonic flow, released instantaneously with zero relative velocity and thereafter allowed to fly freely. A spherical geometry is chosen to avoid the additional complication of induced rotations; however, considering that the physical effects described above are in no way particular to flow about spheres, the results obtained are expected to hold, at least qualitatively, for other regular geometries.

The structure of this article is as follows. In § 2, the experimental facility and apparatus are detailed, including a description of the image-based tracking technique which constitutes the principal measurement method. In § 3, the computational model that is employed alongside the experiments is briefly described. Results of the investigation are presented and discussed in § 4, and conclusions are drawn in § 5.

2. Experimental facility and apparatus

2.1. *Facility*

All experiments were performed in the GALCIT Ludwieg Tube, a schematic of which is shown in figure 2. The facility comprises a 17-meter long tube, an axisymmetric converging-diverging contoured Mach 4 nozzle, a test section and a dump tank. In the present experiments, the diaphragm was placed between the tube and the nozzle, rather than downstream of the test section. The facility is thus said to be run in 'upstream-diaphragm' mode, with the nozzle, test section and dump tank comprising the down-

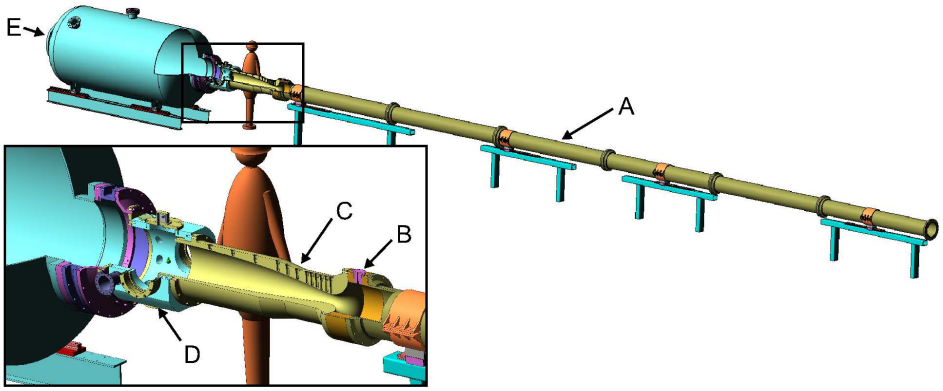

FIGURE 2. Schematic of the GALCIT Ludwieg Tube facility with a blow-up of the test-section region inset: (A) tube; (B) diaphragm holder; (C) converging-diverging Mach 4 nozzle; (D) test section; (E) dump tank.

stream section of the facility. In upstream-diaphragm mode, the flow-establishment time is much reduced, but the passage of the diaphragm fragments through the test section can be problematic: in a number of the present experiments, the fragments struck or influenced the free-flying spheres, in which cases the results had to be discarded.

A test begins by inserting a 0.005-inch thick polycarbonate sheet into the diaphragm holder; the tube and the downstream section are then simultaneously evacuated, typically to 1.5 torr. Thereafter, the downstream section is maintained under vacuum while the tube is filled, quickly to 1.5 bar, then slowly until the diaphragm ruptures. The mean diaphragm burst pressure in the present experiments was 2.27±0.2 bar.

After diaphragm rupture, an expansion wave propagates upstream into the tube, reflects off the end wall, and propagates downstream. The rupture also generates a shock wave that travels into the downstream section; this is partially reflected from the curved nozzle wall, with the main part of the shock simply propagating into the dump tank. The shock is followed by a contact surface which forms the leading boundary of the main test flow. The partially reflected shock continues to create unsteadiness in the test section for a few milliseconds, whereafter the steady test time commences; steady flow ends upon arrival of the reflected expansion wave. Further details regarding the facility can be found in Mouton & Hornung (2008).

2.2. *Free-stream characterisation and measurements*

The free-stream conditions are calculated by considering an unsteady constant-area expansion of the gas in the tube, followed by a steady expansion through the contoured nozzle. First, the Mach number in the tube, M_t, is determined from the area ratio of the tube to the nozzle throat, A_t/A^*:

$$\frac{A_t}{A^*} = \frac{1}{M_t}\left(\frac{\gamma+1}{2}\right)^{-\frac{\gamma+1}{2(\gamma-1)}}\left(1+\frac{\gamma-1}{2}M_t^2\right)^{\frac{\gamma+1}{2(\gamma-1)}}. \tag{2.1}$$

The effective reservoir pressure and temperature, p_0 and T_0, are then calculated in ratio to the fill pressure and temperature, p_f and T_f, respectively:

$$\frac{p_0}{p_f} = \left(\frac{1+\frac{\gamma-1}{2}M_t^2}{\left(1+\frac{\gamma-1}{2}M_t\right)^2}\right)^{\frac{\gamma}{\gamma-1}}, \tag{2.2a}$$

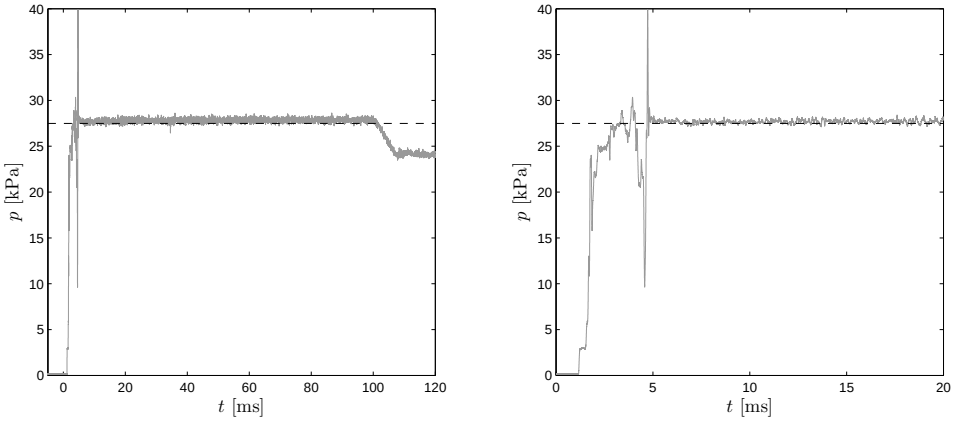

FIGURE 3. A sample Pitot pressure trace of the Ludwieg tube test-section flow: (left) showing the complete steady flow time of the tunnel; (right) showing the typical test duration employed in the present experiments. The dashed line in both plots indicates the theoretical Pitot pressure derived from the fill conditions.

$$\frac{T_0}{T_f} = \frac{1 + \frac{\gamma-1}{2} M_t^2}{\left(1 + \frac{\gamma-1}{2} M_t\right)^2}. \tag{2.2b}$$

The free-stream conditions can then be determined using the steady isentropic one-dimensional relations, assuming a final Mach number of 4.0. Typical conditions for the tests were ρ_∞=0.07 kg m^{-3}, p_∞=1.4 kPa and u_∞=670 m s^{-1}.

To confirm the accuracy of the derived free-stream conditions, a series of Pitot-pressure measurements were performed in the Ludwieg-tube test section. A Pitot probe was designed and instrumented with a Kulite XCS-190-10A-L piezoresistive pressure transducer, running through a Dynamics 7600A signal conditioner. An example of a Pitot pressure trace appears in figure 3: the entire steady flow time of approximately 95 ms is shown in the left plot, while the test duration of ∼20 ms employed for the present tests is shown in the right plot. The start-up period of the flow is seen to last approximately 3.5 ms from the instant the initial shock wave produced by the diaphragm rupture reaches the probe. After flow establishment, the standard deviation in the measured Pitot pressure from the mean value over the steady flow period is less than 1%. In three further Pitot-probe experiments, standard deviations lying between 1 and 2% were recorded.

Also shown in both plots of figure 3 is a dashed line indicating the theoretical value of the Pitot pressure determined from the free-stream conditions and the Rayleigh-Pitot formula. The theoretical result differs from the mean measured value over the entire steady flow period by 1.2%, and by 0.7% between 5 and 20 ms. In the other three Pitot-probe experiments, discrepancies of less than 0.5% were obtained, indicating that the theoretical estimates of the free-stream quantities give good approximations to the actual experimental values.

2.3. *Model arrangement*

The test articles in this study were Nylon 6/6 spheres, ranging in diameter from 1/4 to 1 inch. Several methods of mounting the spheres in the test section were trialled, the intent being to provide a weak suspension that would be detached and swept away during the flow start-up period, imparting a minimal impulse to the spheres. The most effective solution of those tested was found to be suspending each sphere by dental floss from the

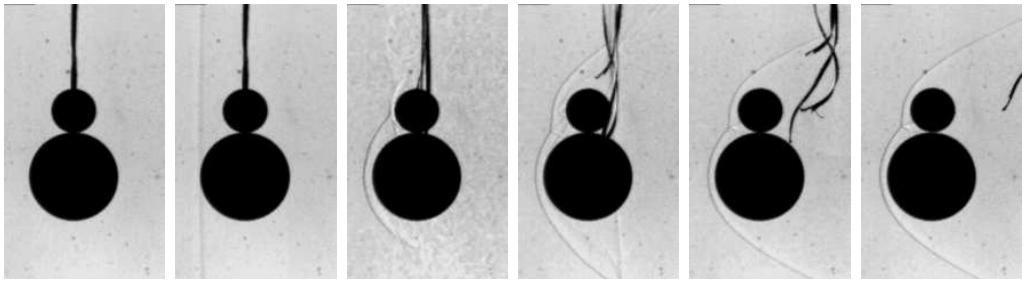

FIGURE 4. Sequence of images showing the start-up of the flow and the detachment of the threads from the spheres, at times (defined from the arrival of the initial shock): -0.08, 0, 0.54, 0.77, 1.00, 1.23 ms.

test section roof, with the attachment formed by melting a single fibre from the frayed floss end to the Nylon body: this ensured the weakest part of the suspension was the link between the body and the tether. Two threads in a V-arrangement were attached to the primary sphere, and a single thread to the secondary sphere. Excrescences of less than 100 microns remained on the sphere surfaces after release. A sequence of shadowgraph images showing the start-up of the flow and the detachment of the threads is presented in figure 4. The arrival of the initial shock and the contact surface are visible in the second and third images, respectively. The thread detachment is completed within 1 ms of the initial shock arrival at the spheres.

2.4. *Visualization setup*

A "focused" shadowgraph optical set-up, consisting of a conventional Z-type Schlieren arrangement with the knife-edge removed, was utilized in this study. Shadowgraphy rather than Schlieren was employed to minimise the influence of the visualised flow features on the tracking technique to be described shortly. The focal lengths of the concave mirrors and the focusing lens were 1.5 m and 75 mm, respectively. The light source was a Ostar four-chip 4000K colour temperature LED mounted to a surplus air-cooled heat sink, driven continuously by a Harrison Laboratories 6267a DC Power Supply. Images were recorded with a Vision Research Phantom V7.1 SR-CMOS monochrome high-speed camera at a resolution of 512×304 pixels; the image magnification was such that a 1-inch diameter sphere (as was generally used for the primary body) had an image diameter of approximately 76 pixels. The frame rate and exposure time were 13 kfps and 2-3 μs, respectively.

Determination of the sphere displacements, velocities and accelerations during separation was performed exclusively through a visualization-based tracking technique. This technique, employed in a basic form in Laurence *et al.* (2007) and subsequently refined in Laurence & Karl (2010) and Laurence (2011), may be summarised as follows. For each image in the recorded sequence, a pixel-resolution Canny edge-detection is performed, and a semi-automated edge-tracing algorithm selects the edge points corresponding to each of the sphere outlines. These edge points are then reprocessed using a subpixel-resolution detector, and the sphere centre-of-mass position, (x_0, y_0), and radius, r, in image coordinates are determined by fitting a circle in the least-squares sense to the calculated points. *A-priori* knowledge of the physical sphere radii then allows the x_0 and y_0 curves to be converted into physical displacements. Velocities and accelerations can be obtained by numerically differentiating the displacement curves; however, the resulting amplification of measurement noise usually means that some form of smoothing is subsequently required, especially for accelerations. Alternatively, if either the velocity or the

acceleration is assumed to be constant over a certain time period, polynomials of first or second order can be fitted to the displacement profiles to yield mean quantities.

For the present work, the large number of images to be processed (typically ∼200 for each experiment) necessitated a higher level of automation than had previously been implemented, particularly in the selection of the sphere edge points. However, it was also desired to mitigate the influence of features such as optical imperfections or impinging shocks that might distort the sphere outlines and were previously excluded manually. Thus, a routine was incorporated whereby, following the first least-squares fit, the radii of all detected points (as measured from the fitted sphere centre) were compared with the overall fitted radius for each sphere, and those exceeding a certain threshold were excluded from a second least-squares fit. A further improvement to the tracking technique was the introduction of a correction for optical distortions, as described in Appendix A.

To estimate the precision of the tracking technique in the present implementation, for each experiment a quadratic polynomial was fitted to the displacement of the primary sphere over the time period that it was outside the domain-of-influence of the secondary sphere, and thus subject to a constant acceleration. We assume that the tracking precision corresponds to the standard deviation of the residuals to this quadratic fit. For a 1-inch diameter sphere, a typical value of 2-3 μm was found; this number can be expected to rise to around 6 μm for 1/4-inch diameter spheres. Although a higher accuracy of ∼1 μm was obtained for sphere measurements under calibrated conditions by Laurence (2011), the present estimate is consistent with both the smaller image sphere diameter and the more challenging experimental conditions here.

2.5. *Analysis of experimental errors*

In this subsection we attempt to characterise both the uncertainties in the experimentally measured quantities and the deviations of the experiments themselves from the model problem of the study, i.e., that of two initially touching spheres released instantaneously and with zero relative velocity in a steady flow. The quantity of principal interest here is the non-dimensional lateral velocity, $v_y' = \sqrt{\rho_m/\rho_a}v_y/V$; thus, we wish to determine the uncertainties in the quantities in this non-dimensional term, as well as those in the independent parameters that are varied in the investigation, namely the radius ratio, r_2/r_1, and the initial alignment angle between the sphere centres, θ_0.

Before each experiment, the diameter and mass of each sphere were precisely measured. The maximum deviation recorded in the sphere diameter from its nominal value was 0.001 inch, giving a maximum discrepancy in the radius ratio ranging from 0.14% for r_2/r_1=1 to 0.6% for r_2/r_1=0.25. The measured diameter and mass were used to determine the average sphere density, ρ_m; this average value, rather than individually measured values, was used in determining each v_y'. Over all spheres, a mean value of 1.122×10^3 kg/m^3 with a standard deviation of 0.4% was obtained. As we have seen in § 2.2, the discrepancy between the measured and theoretically estimated free-stream Pitot pressures, and the variation in the measured Pitot pressure during the test time, were typically less than 1% and 2%, respectively. This is also consistent with measurements of the drag coefficient of the primary spheres during the constant-acceleration sections of their trajectories (the same periods as in the precision estimates described in the last paragraph of the previous subsection), in which a variation of 1.1% was found. Since the Pitot pressure scales as approximately $\rho_a V^2$, the corresponding errors in v_y' from these free-stream uncertainties will be half the values just quoted. From the displacement measurement precision estimated in the previous subsection, the precision in v_y measurements varies from approximately 0.015 m/s for 1-inch diameter spheres to 0.03 m/s for 1/4-inch diameter spheres; corresponding values for the non-dimensional velocity, v_y', are 0.003 and

0.006, respectively. In Appendix A, it is shown that distortions in the optical setup can lead to systematic errors in the determination of v_y of over 1.5%, but with the applied distortion correction, this error is estimated to be less than 0.5%. Additionally, imprecise initial alignment of the spheres in the spanwise direction (i.e., parallel to the light path) will influence the measured lateral velocity; however, the estimated precision of the alignment is of the order of 1°, and even a misalignment of 5° would lead to an error in v_y of less than 0.4%.

The foregoing analysis suggests that the typical uncertainty in the final value of v_y' is of the order of 2%, with the main contribution being uncertainty in the free-stream conditions. Uncertainties in the effective initial conditions, resulting from both the start-up period of the facility and the non-instantaneous detachment of the supporting threads, will also be significant. To determine the impulse imparted by the detaching threads, experiments were performed with a single sphere. The lateral impulse imparted by the single thread suspension was estimated from the measured velocity profiles as approximately 0.12×10^{-4} Ns; the axial impulse could not be separated from the flow-induced loading, but the thread angle during detachment suggested this to be negligible. For sphere diameters of 1, 1/2 and 1/4 inch, this lateral impulse will give rise to velocities of 0.013, 0.1 and 0.6 m/s, respectively; the corresponding non-dimensional velocities are 0.003, 0.02 and 0.12. The V-arrangement suspension, as employed for the primary sphere, was found to impart a somewhat larger impulse: for a 1-inch sphere, the resulting lateral velocity was typically 0.1 m/s. Thus, the assumption of a negligible initial relative velocity was best satisfied for r_2/r_1=0.5; for $r_2/r_1 > 0.5$ the spheres effectively possessed a small negative initial relative velocity (i.e., towards one another) and vice versa.

The influence of the flow start-up period on the effective initial conditions was estimated in the following manner. At the end of the start-up period, the spheres will lie in a particular relative configuration and be carrying certain velocities. Assuming this combination to be given and that both spheres were initially stationary, the effective initial positions of the spheres will depend on the individual acceleration histories. In particular, the initial positions for idealised step-function accelerations (as assumed in the model problem of the study and implemented in the accompanying computations) will differ from those for the actual experimental accelerations. We can quantify this difference if we assume that the force coefficients (based on the instantaneous flow conditions) are approximately constant during the start-up period, and that they are proportional to the measured Pitot pressure. These assumptions are supported by the observation that, in figure 4, the flow structures are well-established within 1.0 ms of the arrival of the initial shock (compared to the entire start-up duration of approximately 3.5 ms). Thus, using the measured Pitot pressure history together with representative force coefficients, we find that, for the experimental acceleration histories, the spheres effectively travel further in reaching the same velocity and that this effect is more pronounced for smaller spheres. This is due to the more gradual onset of aerodynamic loading in experiments and means that, in the idealized model problem approximated by a given experiment, the secondary body has a slightly downstream and laterally separated initial position relative to its actual physical position. This effective initial lateral separation is quite uniform for different r_2/r_1, at 0.3 mm or $0.02r_1$. However, the effective alignment angle discrepancy resulting from the offset in the axial direction varies strongly with r_2/r_1: for r_2/r_1=0.25, 0.5 0.625, 0.75 and 1, the calculated angles are 4.5, 1.4, 0.8, 0.4 and 0°, respectively.

3. Computational modelling

3.1. *Numerical approach*

As in Laurence & Deiterding (2011), we employ the Cartesian fluid solver framework AMROC (Deiterding 2005*b*; Deiterding *et al.* 2005, 2007; Deiterding 2009, 2011*b*,*a*; Ziegler *et al.* 2011) to simulate numerically the fluid-structure interaction of free-flying spherical bodies in supersonic atmospheric flow. The equations solved to model the inviscid compressible fluid are the Euler equations in conservation-law form

$$\partial_t \rho + \nabla \cdot (\rho \vec{u}) = 0, \quad \partial_t (\rho \vec{u}) + \nabla \cdot (\rho \vec{u} \otimes \vec{u}) + \nabla p = 0, \quad \partial_t (\rho E) + \nabla \cdot ((\rho E + p)\vec{u}) = 0. \tag{3.1}$$

Here, ρ is the fluid density, $\vec{u}$ the velocity vector, and E the specific total energy. The hydrostatic pressure p is given by the polytropic gas equation, $p = (\gamma - 1)(\rho E - \frac{1}{2}\rho \vec{u}^T \vec{u})$. We approximate (3.1) in three space dimensions using a discretely conservative Cartesian finite-volume discretisation built on dimensional splitting. The flux vector splitting approach by Van Leer is used to evaluate an upwinded numerical flux at cell interfaces; the MUSCL-Hancock reconstruction technique with Minmod-limiter is employed to construct a high-resolution method that is of second-order approximation accuracy away from shocks and contact discontinuities, cf. Deiterding (2003).

The spherical bodies are represented on the Cartesian mesh with a scalar level-set function, φ, that stores the signed distance to the nearest point on either sphere surface to each finite-volume cell centre. For non-overlapping spheres, the evaluation of φ is straightforward and we adopt the convention $\varphi > 0$ in the fluid domain and $\varphi < 0$ inside the solid bodies. By utilising the sign of φ, the first layer of cells inside each body can be identified; the vector of state in these cells is then adjusted to model the relevant non-Cartesian boundary conditions, i.e., a rigid sphere moving with velocity $\vec{v}$, before applying the unaltered Cartesian finite-volume discretisation. The last step involves the interpolation and mirroring of ρ, $\vec{u}$, and p across the sphere boundary and the modification of the normal velocity in the immersed boundary cells to $(2\vec{v}\cdot\vec{n} - \vec{u}\cdot\vec{n})\vec{n}$, with $\vec{n} = \nabla\varphi/|\nabla\varphi|$, cf. Deiterding (2009). The benefit of this immersed-boundary, aka "ghost fluid" technique (Fedkiw *et al.* 1999) is the natural incorporation of moving bodies. However, the approach usually reduces the approximation accuracy along the immersed boundary, in the present implementation to first order. We mitigate this error by applying automatic, dynamic mesh adaptation along $\varphi = 0$ and additionally to important flow features, specifically to gradients larger than a certain threshold in the fluid density, ρ. A representative snapshot of part of the evolving adaptive mesh from one simulation is visualised in figure 5. The adopted mesh adaptation method is the recursive block-structured algorithm for explicit finite-volume discretisations after Berger & Colella (1988), allowing simultaneous adaptive mesh refinement (AMR) in time and space by the same factor, l_j, for each additional level j. In AMROC, the AMR method is fully parallelised for distributed memory machines, including automatic load-balancing and parallel re-partitioning as the mesh refinement hierarchy changes throughout a computation (Deiterding 2005*a*).

In the simulations described hereinafter, the spheres are always fully enveloped by cells at the highest level of mesh adaptation, and no exchange of kinetic energy by direct contact is allowed to take place. The hydrodynamic force, $\vec{f}$, on each body is updated after every highest-level time step by integrating the pressure over its surface, for the purpose of which spherical longitude-latitude grids are temporarily constructed. The position of each sphere's centre, $\vec{x}$, is then updated by advancing the equation of motion, $\ddot{\vec{x}} = \vec{f}/m$, with mass $m = \frac{4}{3}\pi r^3 \rho_m$. Finally, the level set function is re-calculated taking into account all spherical bodies.

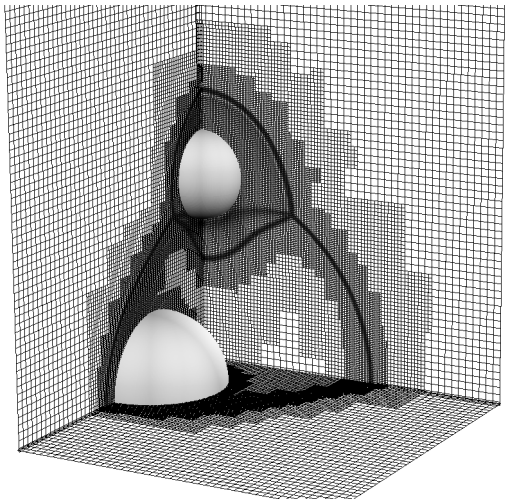

FIGURE 5. Cuts through part of the computational domain of setup 5 described in table 1 at $t = T + 6.4151$, visualising the mesh adaptation around the two bodies together with the shock waves on the cut planes. Two additional levels of refinement with $l_{1,2} = 2$ are used.

3.2. *Model verification*

In order to demonstrate the accuracy and computational performance of the numerical model, here we discuss in detail a series of consecutively refined computations for a specific case of two spheres with a radius ratio $r_2/r_1 = 0.625$ in a Mach-4 flow, corresponding to one of the experiments described in § 4 (see figures 9c and 11). Since it is the non-dimensional results that are ultimately of interest, some freedom exists in setting up the problem. In order to provide a reference and benchmark, we describe the actual configuration simulated.

We study the problem at hand in a Galilean frame of reference and use a computational domain of size $[0, 3] \times [0, 2.5] \times [0.1, 1.9]$. The spheres have radii $r_1 = 0.2$, $r_2 = 0.125$ and their centres are initially located at $(0.35, 1, 1)$ and $(0.3542, 1.3250, 1)$, respectively. The density of both bodies is set to $\rho_m = 2800$ (note that, provided the sphere velocities remain much smaller than the flow velocity, the non-dimensional results are independent of the value of ρ_m/ρ_a). By specifying $\rho_a = 1.4$, $\gamma = 1.4$, uniform initial conditions $\rho_0 = \rho_a$, $\vec{u} = 0$, $p_0 = 1$, and inflow conditions with $\rho_i = \rho_a$ and $p_i = 1$, the magnitude of the inflow velocity vector becomes identical to the Mach number. A $\vec{V}_i = (4, 0, 0)$ inflow is prescribed at the left domain boundary; outflow boundary conditions are applied at all other sides. For $t < 0.25$, the inflow velocity is continuously increased by specifying $\vec{V}_i(1 - \exp(-t/0.05))$ as the boundary condition; for $t \geqslant 0.25$, a constant value of $\vec{V}_i$ is used. The computation is separated into two main parts: during the interval $t = [0, T]$ the spheres are held stationary and a quasi-steady flow field is established; for $t > T$ the two bodies are allowed to move freely according to the experienced forces. The present computation uses $T = 6$ and a final simulated time of $t_e = T + 16$.

The verification study consisted of six simulations with progressively increasing resolution; the relevant computational parameters are provided in table 1. Setups 1 and 2 use uniform grids; setups 3 and 4 employ one additional level of mesh adaptation with refinement factors of 2 and 3; setups 5 and 6 use two additional refinement levels with $l_1 = 2$ and l_2 equal to 2 and 3, respectively. All computations employ automatic time-step adjustment based on a CFL (Courant-Friedrichs-Levy) condition number of 0.9. The computations were run on an IBM BG/P machine, using 128 or 256 processor cores.

#	Base grid	l_1	l_2	$\Delta x_{\min}$	Steps	Time [h]	Cores	CPU [h]
1	$150 \times 125 \times 90$	1	1	0.0200	6,131	7.2	128	918
2	$225 \times 188 \times 135$	1	1	0.0133	9,245	16.8	128	2,151
3	$150 \times 125 \times 90$	2	1	0.0100	12,298	40.4	128	5,176
4	$150 \times 125 \times 90$	3	1	0.0067	18,522	72.4	128	9,271
5	$150 \times 125 \times 90$	2	2	0.0050	24,704	143.8	256	36,808
6	$150 \times 125 \times 90$	2	3	0.0033	37,176	318.3	256	81,474

TABLE 1. Computational parameters of the verification study. Six configurations of successively increased refinement are investigated.

Setup 1 completed in ~ 7.2 hours wall time (~ 918 CPU hours). The largest run, setup 6, computed continuously for almost 2 weeks, requiring $\sim 81,474$ CPU hours. Although this number might appear large, the savings from utilising mesh adaptation are considerable: a uniform computation with the effective resolution of setup 6 would be $6^4 = 1296$ times more expensive than setup 1. Multiplying the setup-1 CPU time yields $1,189,728$ hours or a potential saving from using AMR by a factor of ~ 14.6.

Selected results from the verification study are provided in figure 6 and in tables 2 and 3. In figure 6 are plotted the secondary drag and lift coefficients versus the computational time for the six simulations. Significant oscillations are observed in the profiles from the coarser simulations: these are caused by the effective change in the body geometry as it moves through the Cartesian computational grid, since the surface of the body is only resolved to the grid resolution. A general trend for the force coefficients to decrease in magnitude with increasing resolution is observed. This can be attributed to a decrease in the lateral primary bow-shock displacement as the resolution is increased, as noted in the refinement study of Laurence *et al.* (2007): in the present case, this will lead to an effective increase in the lateral displacement of the secondary sphere relative to the primary shock, resulting in a more rapid expulsion and giving rise to the observed trends in the force coefficients. In tables 2 and 3 are tabulated the x- and y-positions of the secondary and primary spheres, and the velocities and the integral hydrodynamic force components in the x- and y-directions for $t = T + 4$ and $t = T + 12$, respectively. Both sphere centres remain essentially within the plane $z = 1$ throughout all runs and thus, besides some negligible variations to within the accuracy of the numerical method, $v_z \equiv 0$ and $f_z \equiv 0$ can be assumed. Adequate convergence under grid refinement can be inferred from both tables as well as from figure 6.

The standard configuration for the numerical simulations that are compared to experiments in § 4.2 is a two-level computation with $l_{1,2} = 2$, as in setup 5. Quantitative analysis of the grid refinement study suggests that this particular setup evaluates the lateral velocities of the secondary and primary bodies with deviations of less than 3% and 2.5% from the fully converged values. Exemplary flow visualisations from simulation 5 are presented in figure 7. The left column of figure 7 shows planes of pseudo-Schlieren (i.e., velocity gradient magnitude) images perpendicular to the coordinate axes through the sphere centres; the right column visualises the embedded domains covered by the first and second refinement levels using different grey scales, onto which local pseudo-Schlieren visualizations are additionally overlaid. Three exemplary time steps depict the separation of the two bodies and the surfing of the secondary body on the primary bow-shock in three dimensions. To visualise the dynamics of the separation process in better detail, two coloured MPG movies corresponding to the images of figure 7 are included

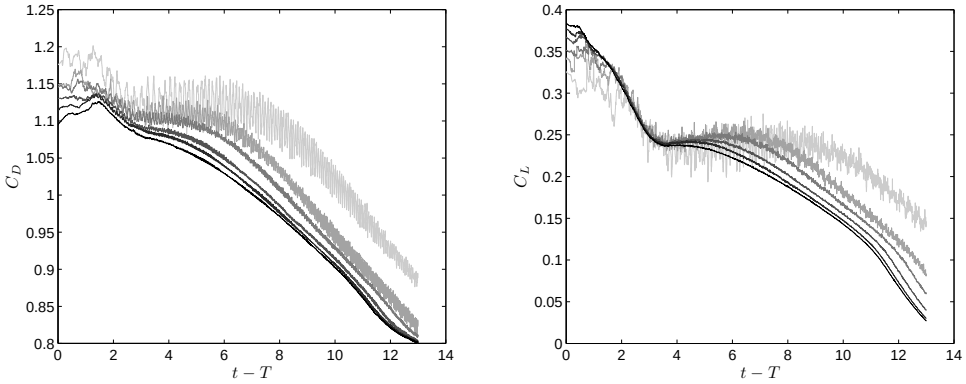

FIGURE 6. Time-resolved force coefficients calculated in the six verification computations described in table 1, with the lightest to darkest curves corresponding to simulations 1 through 6, respectively.

	Secondary						Primary					
#	x	y	$10\,v_x$	$10^2 v_y$	$10\,f_x$	$10\,f_y$	x	y	$10\,v_x$	$10^2 v_y$	f_x	$10^2 f_y$
1	0.5787	1.3821	1.107	2.692	0.6146	1.3372	0.4637	0.9752	0.5552	-0.995	1.2126	-6.237
2	0.5734	1.3864	1.086	2.860	0.6124	1.3337	0.4629	0.9756	0.5531	-0.958	1.2458	-4.358
3	0.5726	1.3875	1.081	2.893	0.6050	1.3211	0.4637	0.9759	0.5570	-0.949	1.2378	-3.654
4	0.5701	1.3887	1.069	2.924	0.5965	1.3238	0.4635	0.9761	0.5565	-0.930	1.2438	-2.881
5	0.5686	1.3892	1.063	2.933	0.5919	1.3191	0.4629	0.9762	0.5549	-0.921	1.2437	-2.499
6	0.5667	1.3895	1.054	2.933	0.5876	1.3070	0.4623	0.9764	0.5529	-0.911	1.2463	-2.056

TABLE 2. Positions, velocities, and integral hydrodynamic force acting on secondary and primary sphere at $t = T + 4$ for the six verification setups.

	Secondary						Primary					
#	x	y	$10\,v_x$	$10^2 v_y$	$10\,f_x$	$10\,f_y$	x	y	$10\,v_x$	$10^2 v_y$	f_x	$10^2 f_y$
1	2.3114	1.7769	3.158	7.040	5.146	0.9521	1.3307	0.8944	1.6109	-1.001	1.1899	0.0968
2	2.2589	1.7954	3.039	6.959	4.768	0.6825	1.3283	0.8986	1.6053	-0.953	1.2057	0.3427
3	2.2396	1.7940	2.999	6.802	4.659	0.5910	1.3352	0.9000	1.6169	-0.938	1.2207	0.2674
4	2.2108	1.7901	2.948	6.611	4.547	0.4738	1.3350	0.9019	1.6172	-0.918	1.2208	0.1671
5	2.1974	1.7864	2.925	6.472	4.539	0.4030	1.3337	0.9030	1.6168	-0.903	1.2209	0.2763
6	2.1821	1.7823	2.903	6.366	4.517	0.3757	1.3316	0.9041	1.6148	-0.892	1.2209	0.2477

TABLE 3. Positions, velocities, and integral hydrodynamic force on secondary and primary sphere at $t = T + 12$ for the six verification setups.

as multimedia attachments to the paper. For reference, these movies additionally display the computational time, t, and the x- and y-coordinates of the sphere centres throughout the entire simulation.

As a first validation result, in figure 8 we compare an experimental Schlieren visualisa-

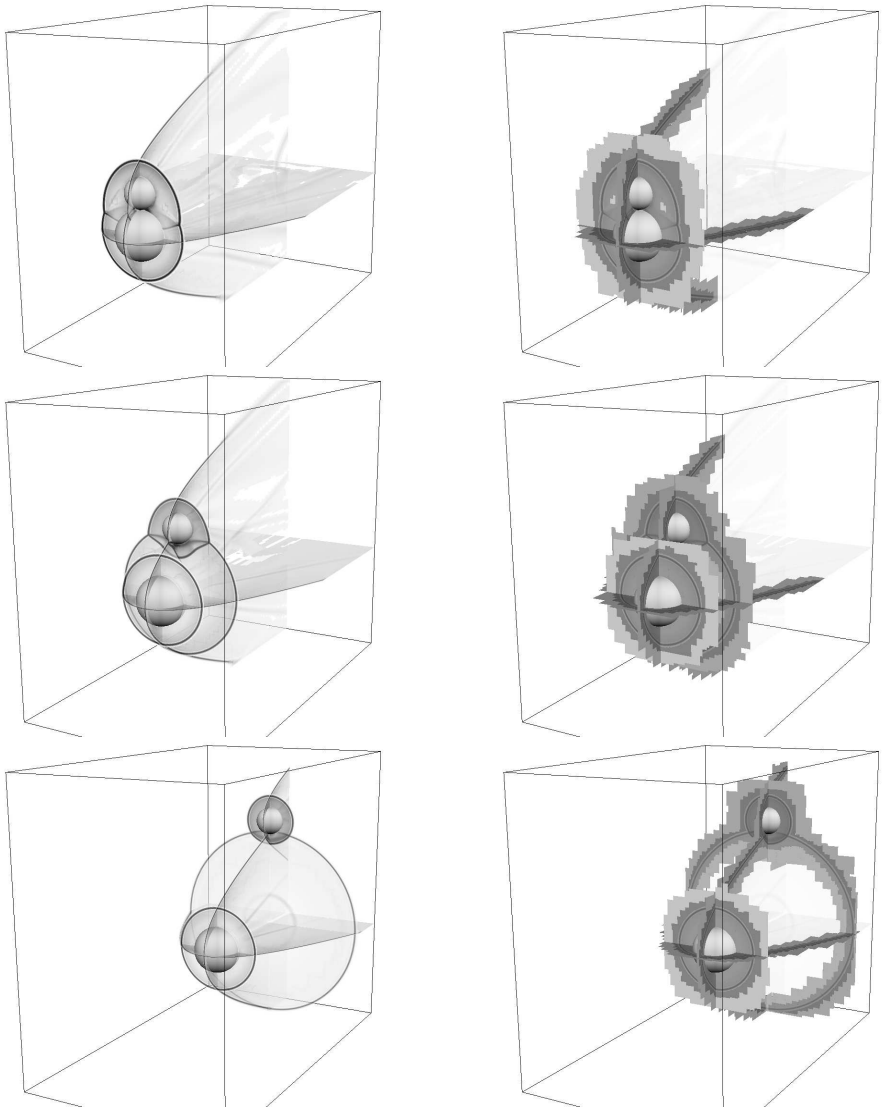

FIGURE 7. Schlieren plots of density (left column) and domains of the two additional AMR levels indicated by different grey scales (right column) for $t = T + 0.17287$ (upper row), $t = T + 6.4151$ (middle), and $t = T + 13.2416$ (bottom), visualising the sphere motions and resulting mesh adaptation dynamics in setup 5.

tion to a similar image derived from simulation 5. For this single experiment, a horizontal knife-edge was placed in the optical path to enable better visualisation of weak features such as the separation regions behind the two spheres. This is simply intended as a qualitative comparison of flow fields, since the configurations are not identical. Moreover, the numerical image visualizes the density gradient in the y-direction only on the central plane, z=1, rather than integrating through the flow domain. Thus, three-dimensional features such as the deflected primary bow-shock following the shock-shock interaction is visible in the experimental image but not in the numerical one. The experimental configuration shows earlier separation on the primary sphere surface, which can be explained by the lack of physical viscosity in the computational model. However, as the

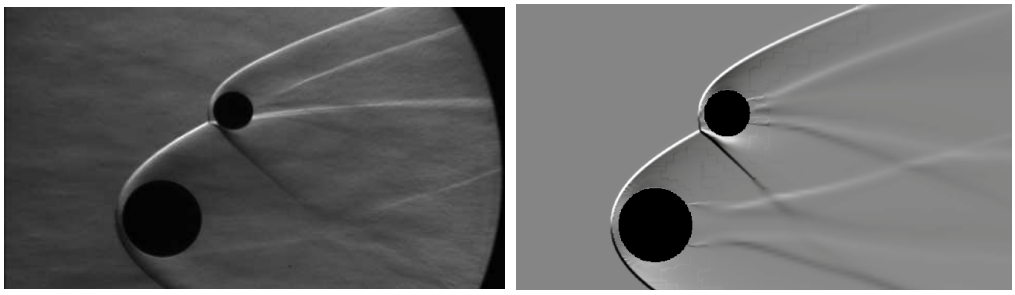

FIGURE 8. Comparison of experimentally and computationally (setup 5, $t = T + 7.8367$) derived visualisations of the gradient of the fluid density in the y-direction. In the experimental image, the gradient has been effectively integrated through the fluid domain in the z-direction, while the computational image shows the gradient only on the central plane, $z = 1$.

aerodynamic forces are dominated at this Mach number by the pressure contribution on the forebody (see, for example, Hoerner (1965)), the differing separation points should have only a minor effect on the experienced forces. Aside from this discrepancy, the qualitative flow features show good agreement: in particular, both images clearly show that the flow in the wake regions is laminar and does not interact with the bow shocks ahead of the bodies. The numerically simulated wake field can be seen particularly clearly in a further colour movie visualising the fluid density in the plane $z = 1$ which accompanies the online version of this paper.

4. Results and discussion

4.1. *Qualitative separation behaviour*

The two parameters varied in the experimental investigation were the radius ratio, r_2/r_1, and the initial alignment angle between the sphere centres, θ_0. In figures 9 and 10 are shown sequences of shadowgraph images from experiments in which each of these two parameters was varied independently of the other. First, in figure 9, we see the effect of varying the radius ratio while the sphere centres are kept initially aligned (to within 1°) in the axial direction. Here the convention adopted for the alignment angle is that θ_0=0 corresponds to exact axial alignment of the sphere centres, with θ_0<0 indicating that the secondary sphere centre initially lies downstream of the primary centre. For r_2/r_1=0.25, the secondary sphere begins fully inside the flow region bounded by the bow-shock of the primary sphere, a configuration that produces a relatively weak repulsive force; thus, the secondary sphere separates very little in the lateral direction and is quickly entrained downstream of the primary bow-shock. If the radius ratio is increased to 0.5, a significantly larger degree of lateral separation takes place, and the secondary body is able to surf the primary bow-shock for a short distance downstream before becoming entrained. For r_2/r_1=0.625, surfing takes place over an extended distance, and the secondary sphere has not yet escaped the influence of the primary bow-shock when it leaves the visualization window, though it is apparent that it will be expelled shortly thereafter. Increasing further to 0.75, the secondary sphere separates quickly in the lateral direction and is soon expelled from the flow region bounded by the primary bow-shock. For r_2/r_1=1, the expected symmetrical separation is observed, with a Mach throat forming between the bow-shocks of the two spheres. Comparing the trajectories for r_2/r_1=0.5 and 0.625, it is apparent that the critical radius ratio delineating entrainment from expulsion lies somewhere between these two values.

Now comparing the sequences in figure 10, the effect of varying only the initial align-

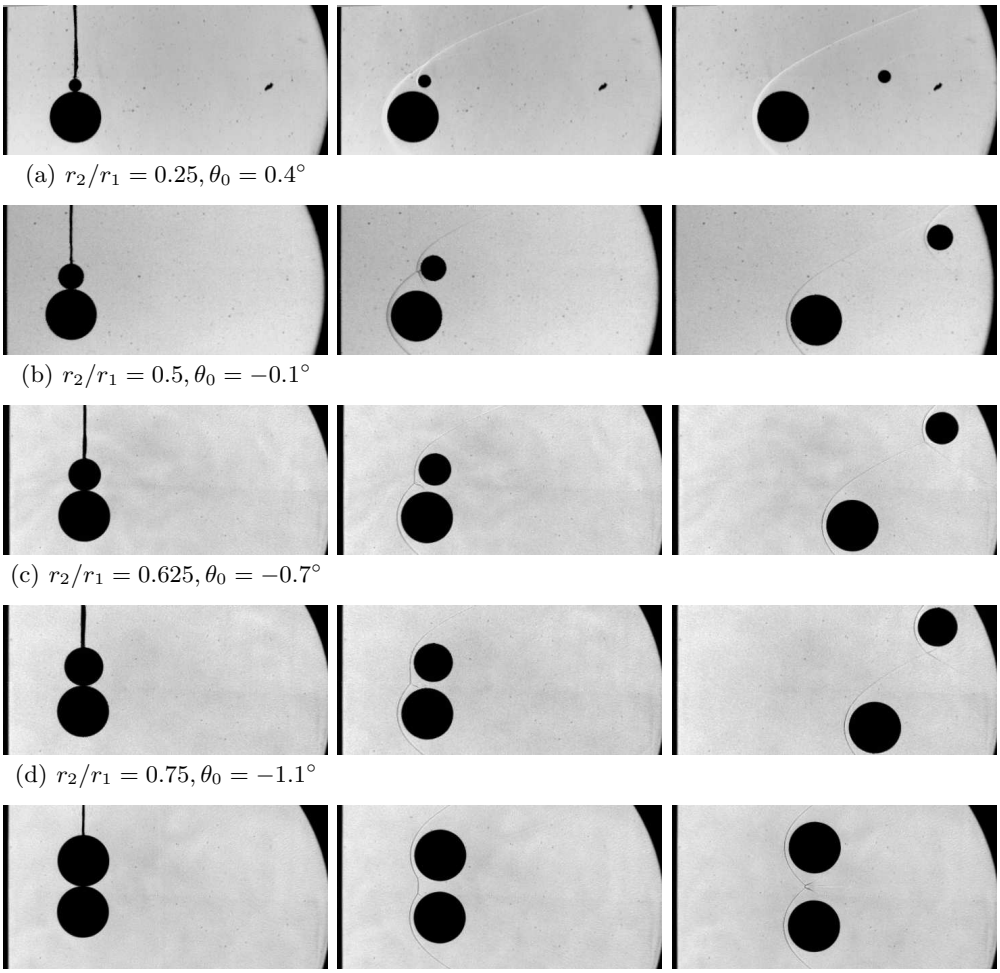

(a) $r_2/r_1 = 0.25, \theta_0 = 0.4^\circ$

(b) $r_2/r_1 = 0.5, \theta_0 = -0.1^\circ$

(c) $r_2/r_1 = 0.625, \theta_0 = -0.7^\circ$

(d) $r_2/r_1 = 0.75, \theta_0 = -1.1^\circ$

(e) $r_2/r_1 = 1.00, \theta_0 = -0.6^\circ$

FIGURE 9. Separation behaviour for configurations with various radius ratios and (approximate) initial alignment of the sphere centres in the axial direction. The duration between the first and last image in each sequence is typically 12 ms.

ment angle between the two spheres may be seen, in this case for r_2/r_1=0.5. Moving the initial secondary position forward relative to the primary sphere (i.e., increasing θ_0) produces a similar effect to increasing the radius ratio, since in either case the secondary body is effectively shifted further outside the primary bow-shock. For both θ_0=-2° and 0, the secondary sphere becomes entrained, slightly more quickly in the former case. Increasing the alignment angle to 4° results in extended surfing of the secondary body, and it is not clear when the body leaves the visualization window whether it will be ultimately entrained or expelled. Increasing θ_0 further to 23° leads to a trajectory similar to that for r_2/r_1=0.75, θ_0=-1.1° (shown in figure 9d), with the secondary body separating rapidly in the lateral direction and soon leaving the influence of the primary shock.

4.2. *Comparison of experimental and computational results*

In this subsection we compare results from selected experiments with those from corresponding numerical simulations. In figure 11, experimental and computational Schlieren

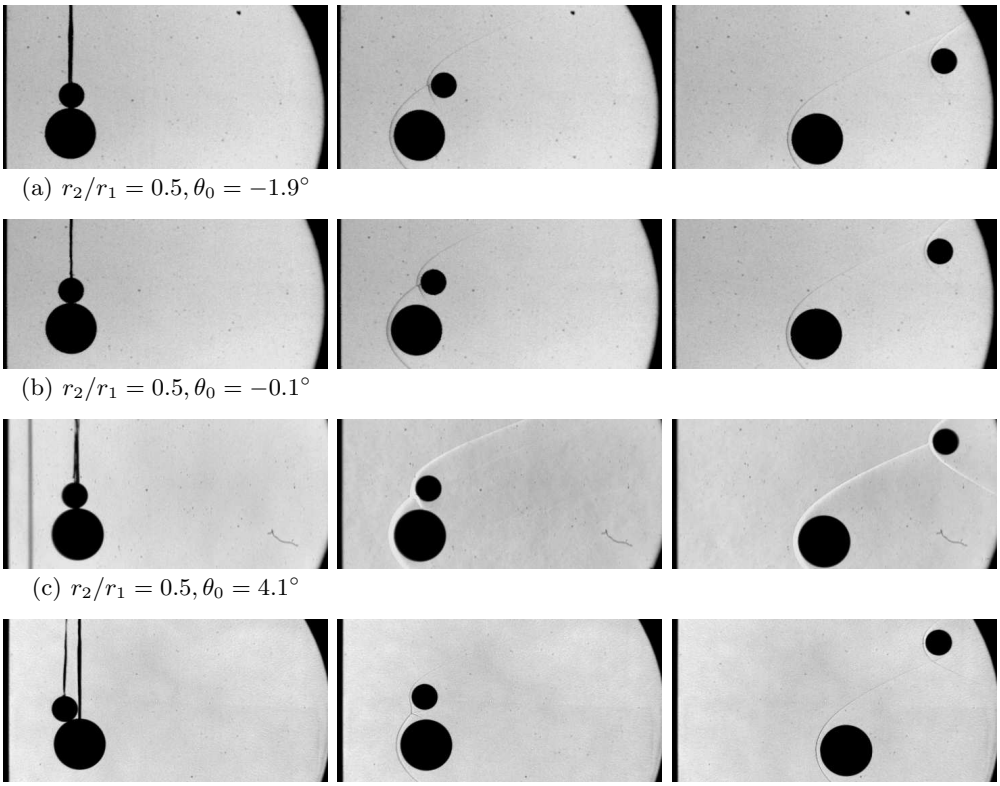

(a) $r_2/r_1 = 0.5, \theta_0 = -1.9°$

(b) $r_2/r_1 = 0.5, \theta_0 = -0.1°$

(c) $r_2/r_1 = 0.5, \theta_0 = 4.1°$

(d) $r_2/r_1 = 0.5, \theta_0 = 22.8°$

FIGURE 10. Separation behaviour for configurations with a constant radius ratio and varying initial alignment angles.

(or pseudo-Schlieren) images are shown for r_2/r_1=0.625, θ_0=-0.7°, i.e., the configuration for the verification study of § 3.2. In this comparison, the non-dimensional time, $t' = \sqrt{\rho_a/\rho_m}tV/r_1$, is matched in each image pair; the respective t'=0 points were determined in a manner outlined shortly. In the computational images, the corresponding experimental sphere positions have been overlaid, with the sphere radii reduced by 10% for clarity. The experimental positions have been corrected to account for the influence of gravity, as is the case for all experimental results presented hereinafter. Qualitatively, agreement between the sphere trajectories is good, with the experimental shock structures accurately reproduced by the computation. However, there is some quantitative disagreement in the sphere positions. The first discrepancy appears in the lateral position of the primary sphere, with the experimental body separating to a lesser extent. The trajectory of the experimental secondary sphere is subsequently affected: it is pushed further outwards laterally and also accelerates more rapidly in the axial direction (these effects can be attributed to the increased lift and drag coefficients experienced by a secondary sphere as it is moved inwards from the free-stream towards the primary bow-shock - see Laurence & Deiterding 2011). The most likely explanation for the initial discrepancy in the primary sphere motion is the lateral impulse imparted by the detaching threads, as discussed in § 2.5.

In figure 12, the time-resolved non-dimensional displacements, non-dimensional velocities and force coefficients are compared for r_2/r_1=0.5, θ_0=-0.1°. The time variable has again been non-dimensionalized to allow an appropriate comparison. In the numerical

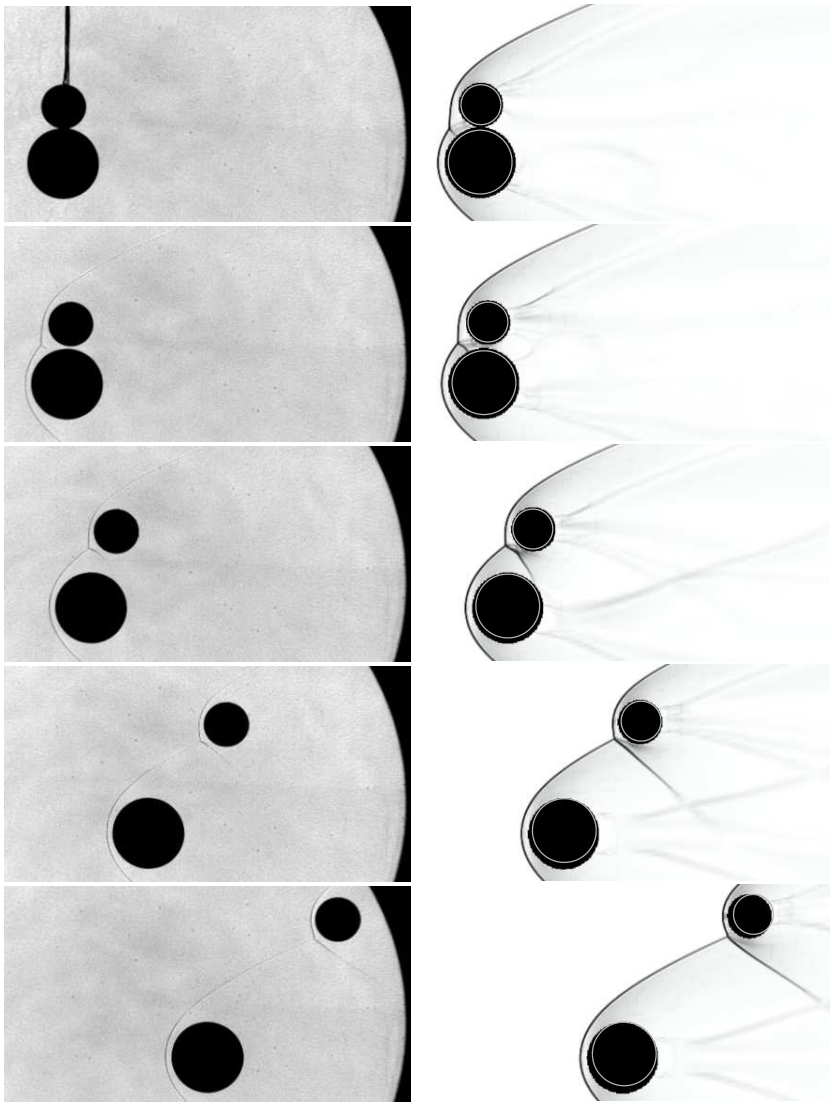

FIGURE 11. Comparison of experimental and computational Schlieren images for r_2/r_1=0.625, θ_0=-0.7°. On the computational images the experimental sphere positions (corrected for gravity) have been overlaid, with the radii reduced by 10% for clarity.

simulation, the instant at which the spheres are released is precisely specified; however, in the experiment the corresponding release instant is not well-defined, due to the finite duration of the flow start-up. As the measured velocities provided the clearest indication of the initiation of the sphere motion, the offset in t' between the two sets of results was chosen such that the initial axial velocity profiles of the primary sphere match as closely as possible. The experimental velocities are derived from the displacement profiles by second-order central differencing, followed by smoothing with a 5-point moving-average filter. The accelerations (from which the force coefficients are derived) are obtained from a second-order central-difference approximation to the second derivative of the displacement data, followed by three consecutive applications of a moving-average filter of widths 15, 9, and 7 points, respectively. Such heavy filtering was necessary to remove the noise

produced by the numerical differentiation, as well as low frequency oscillations that appeared in the acceleration profiles: the origin of the latter was unclear, though they were not present to the same extent in all experiments.

The axial displacement and axial velocity profiles of the primary body show good agreement between experiments and computations. In the drag coefficient profiles, the numerical simulation is seen to underestimate the primary drag by approximately 1.5% following the flow start-up period ($t' \geqslant 1.5$), which may be attributed to the lack of viscous contributions in the computation. We do not expect to obtain agreement in the force coefficients during the start-up period, as the flow conditions have not yet reached the steady values assumed in the derivation of the experimental coefficients. The secondary axial profiles exhibit larger discrepancies than the primary profiles: this is seen most clearly in the drag coefficient, for which the computation lies approximately 6% lower from $t'=1.5$ to 3.5. However, that larger discrepancies are found for the secondary body is not surprising, given that the secondary force coefficients will be much more sensitive to the exact relative positions of the spheres, especially when, in the later stages of the separation, the primary sphere is outside the domain-of-influence of the secondary sphere. The lateral profiles of the primary sphere also show some discrepancies: this appears to result primarily from a deficit in the repulsive force experienced during the flow start-up, again consistent with the impulse imparted by the threads during detachment. Since it is only during the initial stages of the separation that the primary sphere experiences a non-negligible lateral force, these initial effects remain significant in the displacement and velocity profiles in the later stages of the motion. The secondary lateral curves show good overall agreement.

As the secondary lateral velocity is the quantity of principal interest here, in figure 13 we compare time-resolved non-dimensional lateral velocities from experiments and numerical simulations for the five configurations shown in figure 9. Agreement for the smallest radius ratio, $r_2/r_1=0.25$, is seen to be poor. This is due to the low mass of the secondary sphere (0.15 g), which gives rise to both a significant discrepancy in the effective initial alignment angle and a large impulsive velocity imparted by the detaching threads, as discussed in § 2.5. Agreement for $r_2/r_1=0.5$ and 1 is very satisfactory, both in the time development of the velocity profiles and in the maximum velocities attained. However, slightly larger discrepancies are observed for $r_2/r_1=0.625$ and 0.75: while each shows good agreement initially, in the later stages of motion the lateral velocity in the computation decreases more quickly than in the experiment, indicating that the computational secondary sphere is being expelled slightly earlier from the flow region bounded by the primary bow-shock. The origin of this discrepancy for $r_2/r_1=0.625$ has already been discussed in association with figure 11, and the observations made there also apply to $r_2/r_1=0.75$. Nevertheless, agreement for these two cases can still be considered adequate.

Note that for $r_2/r_1=0.25$ and 0.5, the lateral acceleration becomes negative once the secondary sphere is fully entrained within the region bounded by the primary bow-shock, indicating that the lateral force is attractive here. This was predicted theoretically by Laurence *et al.* (2007) and is due to the decreasing effective Pitot pressure moving inwards from the bow-shock towards the axis-of-symmetry of the primary sphere. Thus, the lateral velocity of an entrained secondary sphere reaches a well-defined maximum.

Summarizing these results, with the exception of the $r_2/r_1=0.25$ case, the overall agreement observed between experiment and computations is satisfactory. In particular, we conclude that neither the flow start-up period in the experiments nor the lack of physical viscosity in the numerical simulations are significant obstacles to obtaining meaningful quantitative results in the present investigation.

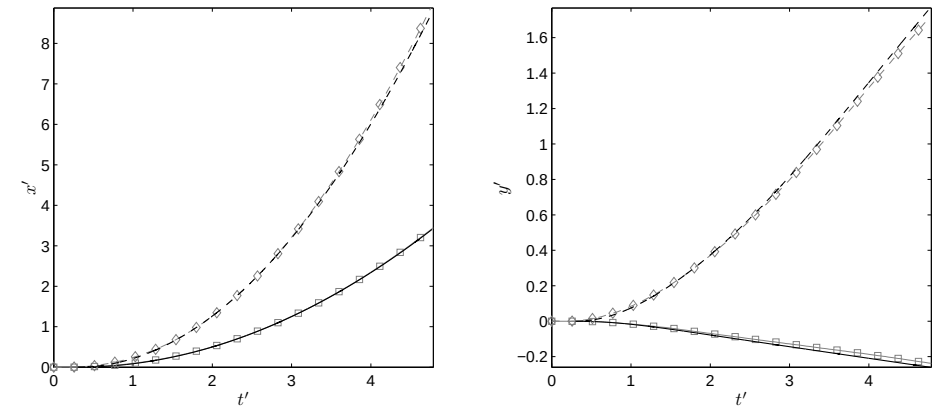

(a) Normalised x- and y-displacements

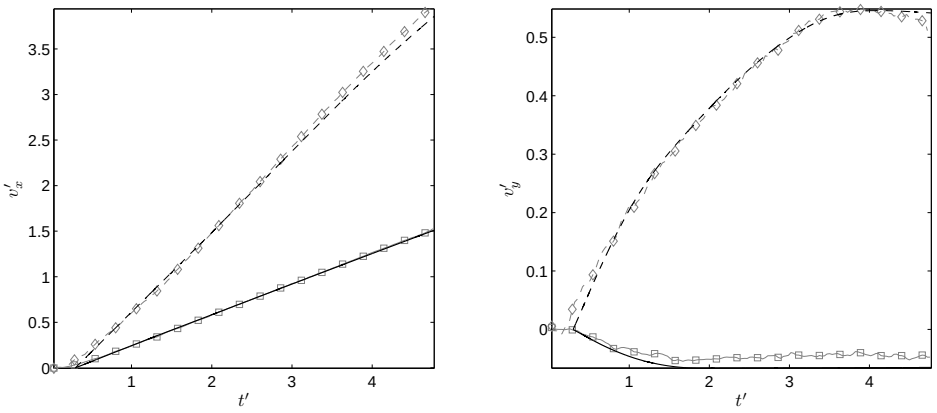

(b) Normalized velocities

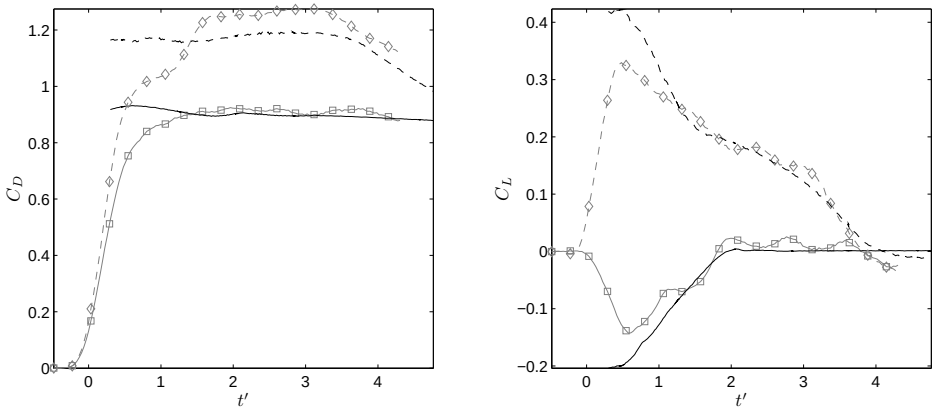

(c) Drag and lift coefficients

FIGURE 12. Comparison of experimental and computational results for r_2/r_1=0.5 and θ_0=-0.1°: —□—, experimental primary sphere; —, computational primary sphere; – –◇– –, experimental secondary sphere; – – –, computational secondary sphere. The normalised variables are: $t' = \sqrt{\rho_a/\rho_m}tV/r_1$, $x' = (x - x(0))/r_1$ and $y' = (y - y(0))/r_1$; $v'_x = \sqrt{\rho_m/\rho_a}v_x/V$ and $v'_y = \sqrt{\rho_m/\rho_a}v_y/V$; $C_D = 8a_x r/(3\rho_a V^2)$ and $C_L = 8a_y r/(3\rho_a V^2)$.

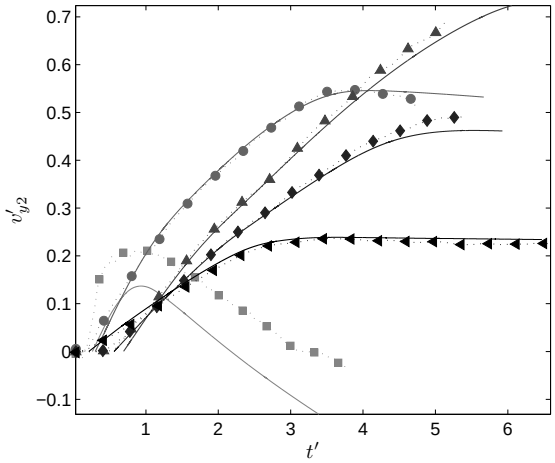

FIGURE 13. Normalised lateral velocities of the secondary body as functions of the non-dimensional time in experiments (symbols) and numerical simulations (lines only in matching shades): □, r_2/r_1=0.25; ○, r_2/r_1=0.5; △, r_2/r_1=0.625; ◇, r_2/r_1=0.75; ◁ r_2/r_1=1.

4.3. *Parameterised separation velocities*

We now consider the quantitative variation in the secondary separation velocity as a function of the two independent parameters, θ_0 and r_2/r_1. In figure 14, the normalised separation velocity, V'_T, is plotted as a function of the initial alignment angle for five radius ratios: $r_2/r_1 = 0.25$, 0.5, 0.625, 0.75, and 1. V'_T, is defined here as the maximum value of $v'_{y2} = \sqrt{\rho_m/\rho_a}v_{y2}/V$ attained during the trajectory. In the left graph are plotted directly measured values: solid points indicate cases in which the secondary sphere was either completely expelled or entrained within the visualized trajectory; open symbols indicate that the secondary sphere was still being repulsed when it left the visualization window and thus had not yet attained a maximum lateral velocity. Each of these open points should thus be considered a lower bound for the separation velocity. In order to estimate the final velocity that would result in each of these cases, the relevant lateral acceleration curve was linearly extrapolated based on the final 3.5 ms of visualized flight; the final separation velocity was then taken as the value at the time at which this extrapolated acceleration became zero. These results are plotted in the right graph of figure 14.

For r_2/r_1=1, V'_T shows only a weak dependence on the alignment angle, increasing from 0.19 for θ_0=15.8° to 0.25 for θ_0=-9.9°. In all of these experiments the two spheres ended up completely outside one another's bow-shock. For r_2/r_1=0.75, a stronger effect of the alignment angle is observed, with V'_T increasing more markedly with decreasing θ_0, but again no secondary entrainment was obtained over the range of initial angles considered (-13.2 to 16.4°). The critical alignment angle delineating entrainment from expulsion for this radius ratio is thus less than -13°. For r_2/r_1=0.5 and 0.625, a well-defined maximum in V'_T, corresponding to the critical value of θ_0, is clearly reached within the range of θ_0 considered: for r_2/r_1=0.5 this occurs at approximately $\theta_0 = 4.1°$, and for r_2/r_1=0.625 somewhere between -6.2 and -0.7°. As θ_0 is decreased from this critical value, entrainment takes over and V'_T drops monotonically. For r_2/r_1=0.25, the secondary sphere was entrained for the three smaller alignment angles and barely expelled at the maximum angle considered (31.6°), indicating that the critical angle lies slightly below this value. We conclude that the critical angle varies strongly with the radius ratio.

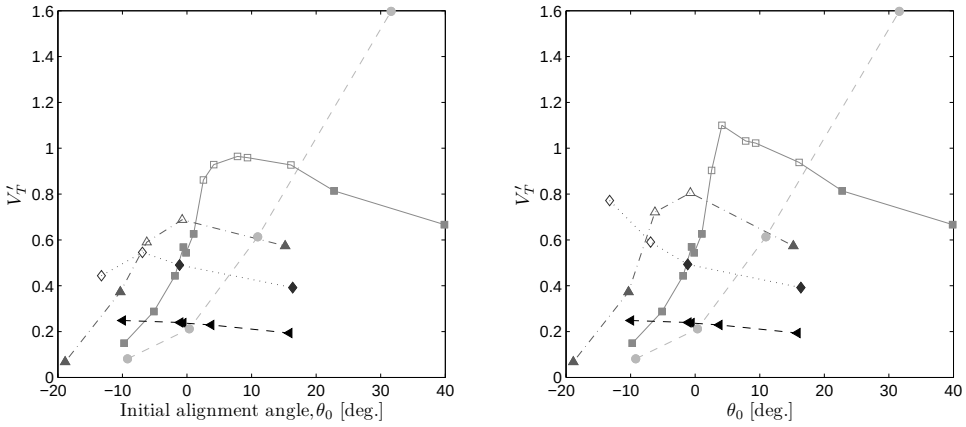

FIGURE 14. Normalised experimental separation velocities of the secondary body as functions of the initial alignment angle with the primary body: ○ r_2/r_1=0.25; □ r_2/r_1=0.5; △ r_2/r_1=0.625; ◇ r_2/r_1=0.75; ◁ r_2/r_1=1. Open points indicate that the secondary body was still being influenced by the primary shock when it left the visualization area: in the left plot these points are the directly measured values, whereas in the right plot they have been extrapolated.

The peak separation velocity attained over all alignment angles is seen to increase with decreasing radius ratio, which can be explained by the higher acceleration experienced by a body of smaller mass, all other things being equal.

In figure 15 the normalised separation velocity is plotted as a function of the radius ratio for axially aligned configurations. Considering the achievable precision in aligning the spheres, here 'axially aligned' indicates an angle of $\theta_0 = 0 \pm 1.5°$; individual values of θ_0 for five of these experiments are given in figure 9. For r_2/r_1=0.625 the extrapolated velocity is used. In addition to the experimental results, also shown are numerical results from the refined computations discussed in § 4.2, in which the same alignment angles as in the experiments were specified, and coarse numerical results in which the alignment angle was set uniformly to θ_0=0. For the coarse simulations, only a single level of grid refinement of factor 2 was employed, and the density ratio, ρ_m/ρ_a, was half the value of the more refined computations. This allowed a larger number of simulations to be performed, providing a clearer trend to the data. As was noted of the qualitative secondary behaviour in § 4.1, the effect of increasing the radius ratio on V_T' is similar to that of making the alignment angle more positive. As r_2/r_1 is increased from 0.25, V_T' increases sharply until a maximum is reached at the critical ratio, predicted by the coarse simulations to lie at approximately 0.58; thereafter, V_T' drops away steeply - more so than in the V_T' versus θ_0 curves in figure 14 - to a value of 0.24 for r_2/r_1=1. This general behaviour is similar to that observed at higher Mach numbers by Laurence & Deiterding (2011).

Comparing the experimental separation velocities with those from the refined numerical simulations, the results are as would be expected from an examination of figure 13. For the smallest radius ratio, r_2/r_1=0.25, the experimental value is significantly higher. The reason for this, namely the low mass of the experimental secondary sphere, has been discussed; an equally light secondary sphere was also employed for the r_2/r_1=0.4 experiment, and a similar discrepancy with the coarse numerical result is observed. For r_2/r_1=0.5 and 1, the experimental and refined numerical results lie very close to one another, but discrepancies are observed at radius ratios of 0.75 and 0.625 of 6% and 11%, respectively (though in the latter case the extrapolation of the experimental result may

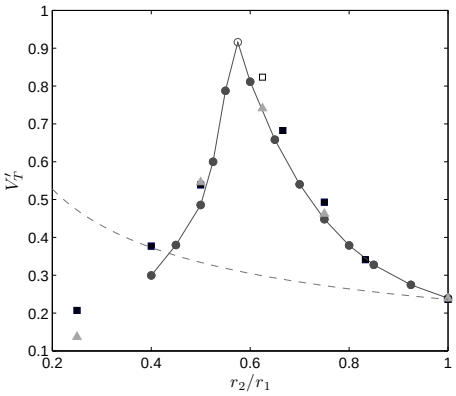

FIGURE 15. Normalised separation velocity of the secondary body as a function of the radius ratio for initial axial alignment of the sphere centres: □, experimental results; △, refined computational result with identical initial alignment angles to experiments; ∘, coarse computational result with θ_0=0; – – –, prediction of Passey & Melosh (1980). Open points indicate extrapolated values.

have exaggerated this difference somewhat.) A likely explanation for these discrepancies has been discussed in reference to figure 13.

Due to differing initial conditions, the refined and coarse numerical results are in most cases not directly comparable. Somewhat surprisingly, however, the largest discrepancy is observed for r_2/r_1=0.5, for which the initial conditions were essentially identical. The reason for this is most likely a slight decrease in the lateral displacement of the primary bow-shock in the more refined simulation, as noted in the verification study of § 3.2. Here this will lead to the secondary sphere becoming entrained more slowly and thus achieving a higher lateral velocity. For r_2/r_1=0.625 and 0.75, the slightly negative initial alignment angle in each of the refined simulations (-0.6 and -1.1°, respectively) will counteract the effect of the reduced lateral bow-shock displacement to some extent, and therefore smaller discrepancies are observed.

Also shown in figure 15 is the scaling law of Passey & Melosh (1980), as given by (1.1). Poor agreement with the experimental and numerical results is observed, and this law clearly fails to predict the qualitative change in separation behaviour that occurs at the critical radius ratio.

4.4. *Effect of Mach number*

It is clear from comparing the results in figure 15 to those in figure 18 of Laurence & Deiterding (2011) that the separation behaviour is qualitatively similar over the range of Mach numbers considered in the two works (M=4, 10 and 25). It is thus of interest to ask what quantitative differences might exist between the supersonic Mach number considered here and the hypersonic Mach numbers of the earlier study. In the left plot of figure 16 are shown the normalised separation velocities as functions of the radius ratio for four Mach numbers, all with θ_0=0: results for M=10 and 25 are taken from Laurence & Deiterding (2011), the coarse-grid M=4 results from figure 15 are again shown, and an intermediate Mach number of 6 is also included. With the exception of the Mach number, all significant parameters in these computations (e.g., grid resolution, density ratio) were identical, allowing the Mach-number effects to be isolated.

Each of the profiles shows the distinctive peak in separation velocity at the critical radius ratio, then a rapid falling off to either side. It should be noted that the M=4 peak

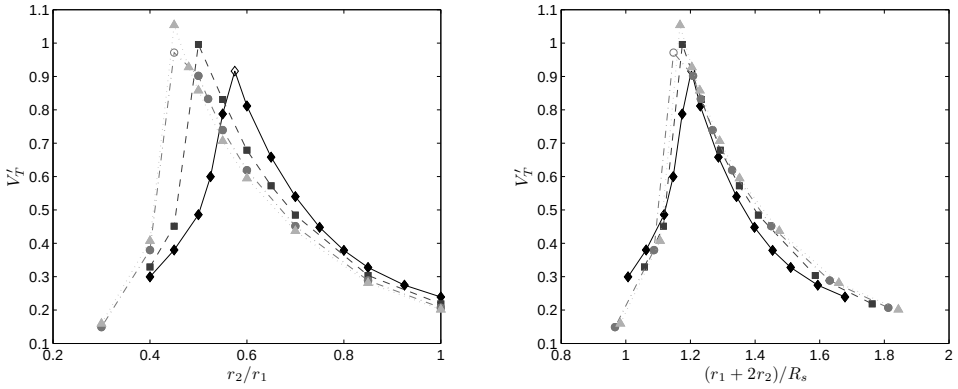

FIGURE 16. Computed normalised separation velocities of the secondary body as functions of the radius ratio for different Mach numbers, assuming initial axial alignment of the sphere centres (θ_0=0): $\diamond$, M=4; $\square$, M=6; $\circ$, M=10; $\triangle$, M=25. In the right plot, the velocity data is plotted against the initial lateral location of the outside edge of the secondary sphere normalised by the lateral primary bow-shock displacement at the relevant Mach number.

is extrapolated; for the M=10 peak, the rate of acceleration was increasing when the secondary sphere left the computational domain, and thus a linearly extrapolated velocity could not be calculated. The value of the critical ratio varies between the different Mach numbers, increasing from approximately 0.45 for M=25 to 0.58 for M=4. This variation can at least be partly explained by the growing lateral displacement of the primary bow-shock with decreasing Mach number: for a larger shock-radius, the secondary sphere will effectively lie further inside the shock for the same initial position, so a larger radius ratio will be required to achieve the same degree of repulsion. Therefore, in an attempt to scale out the effect of the primary bow-shock location, in the right plot of figure 16 are shown the same velocity data, but with the abscissa now the scaled distance $(r_1 + 2r_2)/R_s$, where R_s is the radial location of the primary bow-shock (at the initial axial location of the sphere centres) as given by the correlation of Billig (1967). This variable is thus the initial lateral location of the outer secondary sphere edge, normalised by the bow-shock displacement. With this choice of abscissa the curves collapse much more closely upon one another, suggesting that the Mach-number effect observed in the left plot of figure 16 is indeed primarily due to differences in the effective initial position of the secondary sphere relative to the primary bow-shock.

5. Conclusions

We have carried out an extensive experimental investigation of the separation characteristics of two initially touching spherical bodies in supersonic flow (M=4). In general, the separation behaviour was found to be similar to that observed analytically and computationally at hypersonic Mach numbers (Laurence & Deiterding 2011). For small radius ratios, the secondary sphere is likely to be entrained within the flow region bounded by the primary bow-shock, whereas larger secondary spheres show an increased tendency to be expelled from this region. The likelihood of entrainment increases as the initial position of the secondary sphere is moved downstream relative to the primary sphere. At a critical alignment angle for a given radius ratio (or a critical radius ratio for a given alignment angle), the secondary sphere "surfs" the primary bow-shock, tracing a trajectory so as to follow the shock downstream. This critical angle or ratio effectively

delineates entrainment from expulsion and also results in the maximum separation velocity with respect to the varied parameter. For r_2/r_1=0.5, a critical initial alignment angle of approximately 4° was found (with the secondary sphere centre lying upstream of the primary sphere centre); this critical angle varied strongly with radius ratio, increasing from less that -13° for r_2/r_1=0.75 to approximately 30° for r_2/r_1=0.25. For initial axial alignment of the sphere centres, a critical radius ratio of slightly less than 0.625 was deduced. This critical ratio is larger than that found for higher Mach number flows (approximately 0.45 for $M \geqslant 10$), a difference that was attributed primarily to the increased lateral displacement of the primary bow-shock at lower Mach numbers.

A high-precision visualization-based tracking technique allowed quantitative comparisons between the experimental results and high-resolution numerical simulations. Generally favourable agreement was obtained, the main exception being in the case of low-mass ($< 1\,\mathrm{g}$) secondary bodies, in which case the start-up processes in the experimental facility played a decisive role. This agreement lends a high degree of confidence to both the experimental and computational approaches employed here.

The authors wish to thank Joseph E. Shepherd, whose financial support made the experiments possible, and Hans G. Hornung, with whom useful discussions were had.

Appendix A. Correction of distortion errors

In visualization-based measurement techniques, the distortion error associated with the optical set-up can often be problematic. With regard to the technique employed in the present work, optical distortions were noted by Laurence & Karl (2010), but their effect on the tracking technique could not be quantified beyond a rough estimate. Here, with the relatively large range of motion experienced by the spheres, such distortions were found to become a significant factor, and an attempt was made to both characterize and correct for the resulting errors. To this end, a transparent plate with circular dimples precision-machined at 1-inch intervals was placed in the test section, and images were recorded with the optical set-up employed for the sphere experiments. The visualized positions of the dimples were determined using the tracking routine described in § 2.4, and compared to a uniform grid. A third-order polynomial transformation between image coordinates, $(\hat{x}, \hat{y})$, and physical coordinates, (x, y), was then defined for each of x and y, e.g., $x = a + b\hat{x} + c\hat{y} + d\hat{x}^2 + e\hat{x}\hat{y} + f\hat{y}^2 + g\hat{x}^3 + h\hat{x}^2\hat{y} + i\hat{x}\hat{y}^2 + j\hat{y}^3$, and the coefficients were determined by a least squares fit over all the determined dimple positions. In this way, rather than by directly interpolating between the dimple positions, the influence of individual position errors was minimized.

With the coefficients for each of x and y thus calculated, the correction was incorporated into the tracking algorithm by applying it to the detected edge points prior to the fitting of the circular profile. Applying the transformation directly to the image would also be possible, but would be more expensive computationally. A typical reduction in the distortion of the sphere profiles enabled by this correction is shown in figure 17. The deviation between the radii of the detected edge points and the overall fitted radius is plotted here against the internal angle, ϕ, for each of the two spheres in the image shown (normalised by the fitted radius in each case), for both the original and corrected edge points. The deviation for the larger sphere, which originally reaches 1%, is reduced by a factor of approximately 10, while for the smaller sphere the reduction is by a factor of 6. Furthermore, the root-mean-square (RMS) deviation in both cases is now approximately 0.03 pixels (Laurence & Karl 2010), which is close to the expected accuracy of the edge

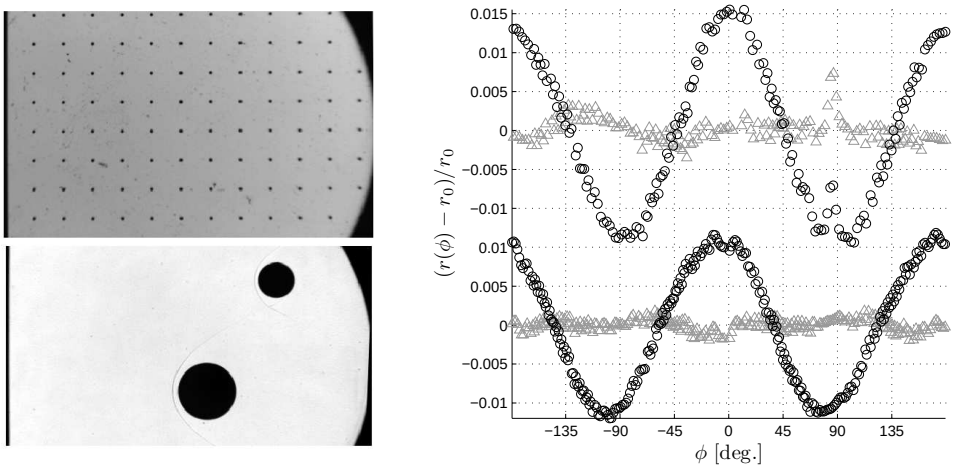

FIGURE 17. (Left) Images showing the transparent grid used to derive the correction polynomials for optical distortions, and the sphere configuration for which the distortion error is quantified in the accompanying plot. (Right) Distortion errors in the measured sphere edge points for the primary body (lower profiles) and secondary body (upper profiles): ∘ uncorrected image; △ image with distortion correction applied. The anomaly in the corrected secondary profile at 90° is due to the excrescence from the suspension thread.

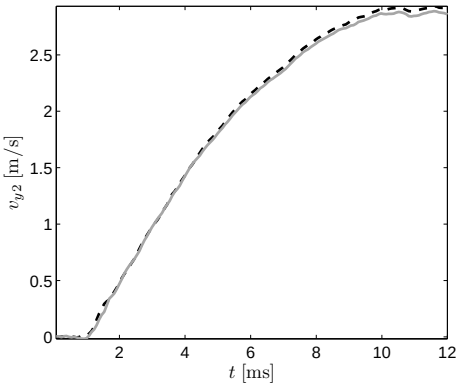

FIGURE 18. Example of the effect of the distortions present in the optical system on the measured lateral velocity of the secondary body: − − −, corrected; —, uncorrected.

detection routine under noisy conditions; or 10 μm, which is near the quoted sphericity of the spheres employed (0.005”).

As the quantity of main interest in the present study is the lateral separation velocity of the secondary body, in figure 18 is plotted an example of a time-resolved lateral velocity profile, both with and without the distortion correction incorporated into the measurements. The discrepancy between the two results is initially negligible, but grows to 1.7% by the time the maximum lateral velocity is reached. As the correction employed has already reduced the error in the sphere profile by a factor of 6, we can roughly estimate the remaining velocity error to be of the order of 0.3%. Given the other experimental uncertainties discussed in § 2.5, any further improvement to the distortion correction is unlikely to offer significant benefits.

REFERENCES

Artem'eva, N. A. & Shuvalov, V. V. 1996 Interaction of shock waves during the passage of a disrupted meteoroid through the atmosphere. *Shock Waves* **5**, 359–367.

Artemieva, N. A. & Pierazzo, E. 2009 The Canyon Diablo impact event: projectile motion through the atmosphere. *Meteorit. Planet. Sci.* **44** (1), 25–42.

Artemieva, N. A. & Shuvalov, V. V. 2001 Motion of a fragmented meteoroid through the planetary atmosphere. *J. Geophys. Res.* **106** (E2), 3297–3309.

Berger, M. & Colella, P. 1988 Local adaptive mesh refinement for shock hydrodynamics. *J. Comput. Phys.* **82**, 64–84.

Billig, F. S. 1967 Shock-wave shapes around spherical- and cylindrical-nosed bodies. *J. Spacecraft Rockets* **4** (6), 822–823.

Bland, P. A. & Artemieva, N. A. 2003 Efficient disruption of small asteroids by Earth's atmosphere. *Nature* **424**, 288–291.

Bland, P. A. & Artemieva, N. A. 2006 The rate of small impacts on Earth. *Meteorit. Planet. Sci.* **41** (4), 607–631.

Borovička, J. & Kalenda, P. 2003 The Morávka meteorite fall: 4 Meteoroid dynamics and fragmentation in the atmosphere. *Meteorit. Planet. Sci.* **38** (7), 1023–1043.

Chyba, C. F., Thomas, P. J. & Zahnle, K. J. 1993 The 1908 Tunguska explosion: atmospheric disruption of a stony asteroid. *Nature* **361**, 40–44.

Deiterding, R. 2003 Parallel adaptive simulation of multi-dimensional detonation structures. PhD thesis, Brandenburgische Technische Universität Cottbus.

Deiterding, R. 2005*a* Construction and application of an AMR algorithm for distributed memory computers. In *Adaptive Mesh Refinement - Theory and Applications, Lecture Notes in Computational Science and Engineering 41*, pp. 361–372.

Deiterding, R. 2005*b* Detonation structure simulation with AMROC. In *High Performance Computing and Communications 2005, Lecture Notes in Computer Science 3726*, pp. 916–927.

Deiterding, R. 2009 A parallel adaptive method for simulating shock-induced combustion with detailed chemical kinetics in complex domains. *Computers & Structures* **87**, 769–783.

Deiterding, R. 2011*a* Block-structured adaptive mesh refinement - theory, implementation and application. *ESAIM Proc.* **34**, 97–150.

Deiterding, R. 2011*b* High-resolution numerical simulation and analysis of mach reflection structures in detonation waves in low-pressure $H_2 : O_2 :$ Ar mixtures. *J. Combustion* **2011**, 738969.

Deiterding, R., Cirak, F., Mauch, S.P. & Meiron, D.I. 2007 A virtual test facility for simulating detonation- and shock-induced deformation and fracture of thin flexible shells. *Int. J. Multiscale Computational Engineering* **5** (1), 47–63.

Deiterding, R., Radovitzky, R., Mauch, S. P., Noels, L., Cummings, J. C. & Meiron, D. I. 2005 A Virtual Test Facility for the efficient simulation of solid materials under high energy shock-wave loading. *Engineering Comput.* **22** (3–4), 325–347.

Fedkiw, R. P., Aslam, T., Merriman, B. & Osher, S. 1999 A non-oscillatory Eulerian approach to interfaces in multimaterial flows (the ghost fluid method). *J. Comput. Phys.* **152**, 457–492.

Hills, J. G. & Goda, M. P 1993 The fragmentation of small asteroids in the atmosphere. *Astron. J.* **105** (3), 1114–1144.

Hoerner, S. F. 1965 *Fluid-Dynamic Drag: Practical Information on Aerodynamic Drag and Hydrodynamic Resistance*. Hoerner Fluid Dynamics.

Laurence, S.J. 2011 On the tracking of rigid bodies through edge-detection and least-squares fitting. *Exp. Fluids* .

Laurence, S.J. & Karl, S. 2010 An improved visualization-based force-measurement technique for short-duration hypersonic facilities. *Exp. Fluids* **48** (6), 949–965.

Laurence, S. J. & Deiterding, R. 2011 Shock-wave surfing. *J. Fluid Mech.* **676**, 396–431.

Laurence, S. J., Deiterding, R. & Hornung, H. G. 2007 Proximal bodies in hypersonic flow. *J. Fluid Mech.* **590**, 209–237.

Mouton, C. A. & Hornung, H. G. 2008 Experiments on the mechanism of inducing transition between regular and Mach reflection. *Phys. Fluids* **20**, 126103.

Passey, Q. R. & Melosh, H. J. 1980 Effects of atmospheric breakup on crater field formation. *Icarus* **42**, 211–233.

Svetsov, V. V., Nemtchinov, I. V. & Teterev, A. V. 1995 Disintegration of large meteoroids in Earth's atmosphere: theoretical models. *Icarus* **116**, 131–153.

Ziegler, J.L., Deiterding, R., Shepherd, J.E. & Pullin, D.I. 2011 An adaptive high-order hybrid scheme for compressive, viscous flows with detailed chemistry. *J. Comp. Physics* **230** (20), 7598–7630.